

Journal of Fluid Mechanics

<http://journals.cambridge.org/FLM>

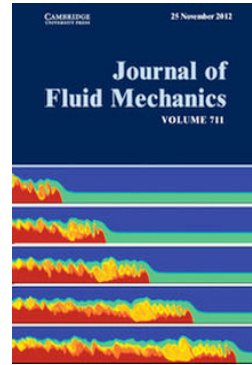
Additional services for *Journal of Fluid Mechanics*:

Email alerts: [Click here](#)

Subscriptions: [Click here](#)

Commercial reprints: [Click here](#)

Terms of use : [Click here](#)



The initial response of a stratified lake to a surface shear stress

Craig Stevens and Jörg Imberger

Journal of Fluid Mechanics / Volume 312 / April 1996, pp 39 - 66

DOI: 10.1017/S0022112096001917, Published online: 26 April 2006

Link to this article: http://journals.cambridge.org/abstract_S0022112096001917

How to cite this article:

Craig Stevens and Jörg Imberger (1996). The initial response of a stratified lake to a surface shear stress. *Journal of Fluid Mechanics*, 312, pp 39-66 doi:10.1017/S0022112096001917

Request Permissions : [Click here](#)

The initial response of a stratified lake to a surface shear stress

By CRAIG STEVENS† AND JÖRG IMBERGER

Department of Environmental Engineering, and Centre for Water Research,
University of Western Australia, Nedlands, WA, Australia, 6009

(Received 15 August 1991 and in revised form 20 September 1995)

Laboratory experiments are used to study the initial response of a stratified fluid to the action of a wind stress. The experiments are described in the context of a parameterization scheme that quantifies the strength of the applied stress relative to the bulk stability of the fluid and also the duration of the wind stress relative to the periods of the waves generated by the stress. This study concentrates on the first fundamental internal wave period in experiments where the fluid is considered to have upwelled, i.e. the stratified region of the fluid reaches the surface at the upwind endwall. The majority of the experiments use three-layer initial density profiles as an approximation to a continuously stratified water column.

A linear model using normal modes proved successful prior to the commencement of upwelling and this enabled an estimate to be made of the time at which upwelling occurred. At this point the wave development ceased and the flows developed via entrainment mechanisms. Consideration of the energy budget showed that little of the input energy was stored in the system. The initial mixing efficiency, defined as the ratio of the mean potential energy gained to the energy imparted by the belt, never exceeded 30%. Peak efficiency occurred when the surface stress was just sufficient to bring the interfacial region to the surface.

1. Introduction

Most natural water bodies are stratified in some way. While stratification might involve a range of properties including temperature and chemical composition, the general result is a density stratification which resists vertical mixing. Knowledge of this stratification and mixing has direct application to lakes where, in a broad sense, transport between the photosynthetically active, oxygen-rich, surface waters and the nutrient laden benthos, controls the ecology of the lake (Stumm 1985). Wind action at the free-surface of the lake injects energy into the water column and thus generates surface and internal waves as well as mean circulation and turbulence, all of which can lead to vertical mixing. This paper describes internal wave phenomena occurring as the wind field commences.

The simplest stratified water body is a two-layered fluid (figure 1) in which vertical transport involves either a change in the depth of the interface or changes in properties of one or both of the layers, or the two effects together. Understanding of the vertical transport evolved from an oceanographic context (e.g. Wu 1973) which did not necessarily require vertical boundaries. The addition of confining endwalls results in the generation of a longitudinal pressure gradient as the wind forces the fluid against

† Present address: Department of Civil Engineering, The University of British Columbia, V6T 1Z4, B.C., Canada.

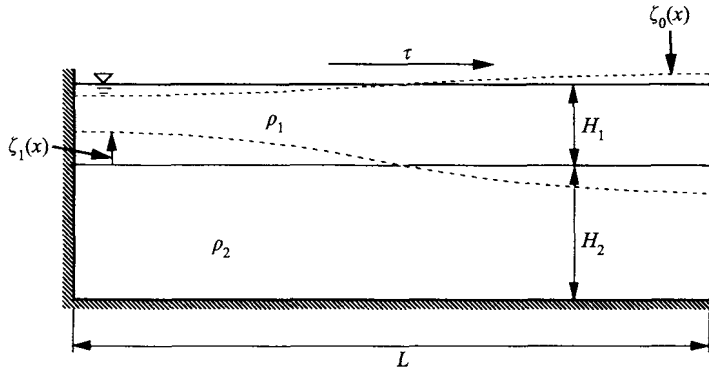


FIGURE 1. Schematic diagram for a two-layered stratified fluid.

the down-wind boundary. The density stratification response to the forcing, but as it is generally a thousand times weaker than the density step at the air–water interface, it does so more slowly and with greater vertical excursion (Hellström 1941; Mortimer 1953). Resultant temperature fluctuations associated with this have long been observed (e.g. Wedderburn 1912) and have been described as an internal seiche, although this does not necessarily imply simple sinusoidal displacements (in space and time) from equilibrium (Thorpe 1977).

Laboratory observations of Wu (1973) and Kranenburg (1985) showed how wind acting on a two-layered fluid generates an interfacial tilt which is inversely proportional to the stability of the surface layer. The stability of the surface layer, of undisturbed thickness h_1 , is parameterized by a bulk Richardson number Ri given by

$$Ri = \frac{\epsilon g h_1}{u_*^2}, \quad (1)$$

where the reduced gravity, $\epsilon g = (\Delta\rho/\rho_0)g$, is the vertical acceleration due to gravity g , factored by the density step at the interface $\Delta\rho$, non-dimensionalized with respect to a reference (average) density ρ_0 . The forcing is represented by the friction velocity $u_* = (\tau/\rho_0)^{1/2}$ where τ is the surface stress. The longitudinal (x -direction) gradient of the interface perturbation from quiescent conditions, denoted ζ_1 , is

$$\frac{\partial \zeta_1}{\partial x} = Ri^{-1}. \quad (2)$$

The evolution from oceanographic conditions retained an emphasis on processes that dominate in the ocean, namely stirring and shear-driven mixing. Given vertical confines, Spiegel & Imberger (1980) indicated that it was possible to generate a tilt (2) sufficient to bring the interface to the surface at the upwind end of the fluid; this is termed upwelling.

Thompson & Imberger (1980) and Monismith (1986) subsequently used numerical and laboratory experiments to model the interfacial tilting. They introduced the Wedderburn number,

$$W = \frac{h_1}{L} Ri \quad (3)$$

that uses the surface layer aspect ratio (h_1/L where L is the longitudinal extent of the basin) to identify whether the tilt described by (2) is sufficient for upwelling to occur.

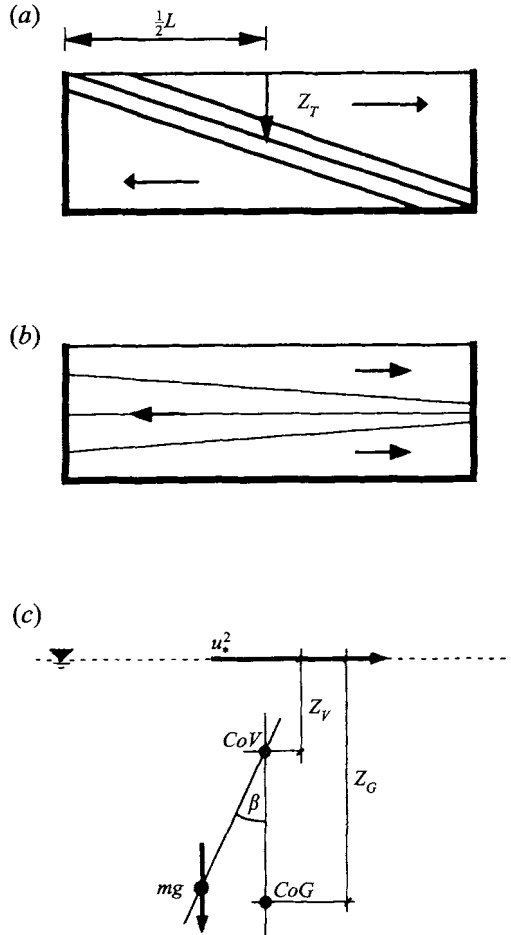


FIGURE 2. Diagram showing the behaviour of the intermediate region for vertical modes (a) one and (b) two, and (c) how the moments are calculated for the L_N model.

Thus, a wind too weak to generate upwelling in a given stratified confined fluid is identified by $W \gg 1$, whereas the opposite condition, where upwelling presumably dominates, occurs when $W \ll 1$. The transition point where upwelling just occurs is $W \simeq 1$ (Thompson & Imberger 1980), although strictly, given a constant $\partial \xi_1 / \partial x$, the idealized transition point is $W = 0.5$. Monismith (1986) found that fluid from the lower layer and the interface region appeared at the upwind surface region for values of W as high as 5. This was attributed to departure from constant $\partial \xi_1 / \partial x$ and the effect of a finite interface thickness that allowed more than one vertical wave-mode to form. Figures 2(a) and 2(b) illustrate the effect of the first two vertical wave modes. Imberger & Patterson (1989) defined what is effectively an integral equivalent to W as the so-called Lake number L_N which is defined by:

$$L_N = \frac{M_{bc}}{\tau A z_V}, \quad (4)$$

where M_{bc} is the baroclinic moment, about the centre of volume, of the water column if the density structure were at the point of upwelling, A is the surface area of the fluid over which τ acts and z_V is the lever arm for the moment generated by the stress which

Location	Date d-m-y	T_w (h)	T_1 (h)	L_N	L (km)	Reference
Kootenay Lake	27-7-77	42	130	6	140	Carmack <i>et al.</i> (1986)
Loch Earn	13-9-51	8	14	1.5	7	Heaps & Ramsbottom (1966)
Wellington Reservoir	13-3-82	8	12	1	1.5	Imberger (1985)
Lake Kasumigaura	29-8-87	5	55	0.3	10	Ishikawa & Tanaka (1993)
Frains Lake	1-7-77	~ 5	3	12	0.4	La Zerte (1980)
Wellington Reservoir	11-3-82	17	4	3	1.5	Monismith (1985)
Alpernacher See	15-7-89	10	6	0.7	3.5	Münnich <i>et al.</i> (1992)
Loch Ness	6-9-73	20	54	1	35	Thorpe (1977)
Gersauersee	25-3-88	12	60	1.5	8	Van Senden & Imboden (1989)
Wood Lake	8-8-82	~ 10	10	13	7	Wiegand and Chamberlain (1987)

TABLE 1. Tabulated list of observations from relevant field experiments including our estimates of the wind duration, T_w , the first internal mode period T_1 , L_N and the horizontal lengthscale, L , for typical wind events

is the distance from the water surface to the centre of volume. For the two-layer case, this parameter has effectively the same numerical meaning as W , so that when the moment due to the wind-forcing equals that generated by a upwelling fluid then $L_N = 1$; increasing the wind results in L_N dropping below unity. The advance of L_N over W lies in the integral nature of the L_N quantity so that any continuous stratification can be incorporated without ambiguity and deep upwelling can be differentiated from upwelling of the diurnal surface layer.

A crucial point when considering the usefulness of W and L_N is that they are steady-state parameters. As the response is characterized by an internal standing wave of the gravest horizontal mode, the long-wave speed $c_l = (g h_1 h_2 / (h_1 + h_2))^{1/2}$ limits the rapidity of the tilting. Spigel & Imberger (1980) showed that, after commencement of the stress, it takes $\frac{1}{4}$ of the internal wave period

$$T_1 = 2L/c_l \quad (5)$$

for the condition identified by W to occur. Furthermore, the response overshoots and, in the absence of friction, peaks at a slope twice that of Ri^{-1} at time $\frac{1}{2}T_1$. Examination of field observations indicates that forcing durations do not always reach typical values of T_1 (table 1). Observations (Heaps & Ramsbottom 1966; Stevens *et al.* 1996) indicate that seiches only persist for a few wave periods so that forcing almost never lasts long enough to generate a steady-state flow.

The work presented here uses laboratory techniques to collect data in the initial period of experiments where upwelling occurs. The objective is to examine the deficits of the parameterization scheme, namely the non-steady behaviour and finite interfaces and indicate improvements to the scheme. The use of an instrumented belt to measure stress, and image processing to estimate velocities, provided data not previously collected in this type experiment.

2. Parameterization and modelling

In an effort to confine the problem, the study was limited to a rectangular basin where the wind stress was considered to be evenly distributed over the water surface. Effects of the earth's rotation were ignored, limiting the direct applicability of the results to small, or narrow, water bodies. Finally, the mean flow was assumed to be two-dimensional; the generality and validity of this assumption is examined in §4.2.

2.1. 'Steady state' parameters

Calculation of the L_N comparison of moments required several assumptions to be made; the first being, at the point of upwelling, the stratification has rotated as if it were purely driven by the first mode dynamics. Mortimer's (1953) observations of a three-layer system showed that the steady state consisted of an upper interface tilted as in (2) and a undeflected lower interface, so that the L_N does not strictly represent steady conditions. Secondly, a consistent position within the stratification must be defined that identifies when upwelling has occurred. Imberger & Patterson (1989) labelled this depth z_T and specified it as the middle of the density gradient region. This is illustrated by figure 2(a), where the isotherms tilt in such a way that the middle of the interfacial region just reaches the surface at the upwind end.

The baroclinic moment M_{bc} is an integral quantity based on the perturbation of the density from the minimum density of the water column at the unforced equilibrium state. Thus, the vertical integrated mass differential per unit width is given by,

$$m = \int_0^H L[\rho(H) - \rho(z)] dz,$$

where H is the full depth of the water column and $\rho(H)$ is the fluid of maximum density in the water column. The M_{bc} is the product of m and the lever arm representing the horizontal displacement of the centre of gravity of the water column from a vertical line passing through the centre of volume. The force/lever arm diagram, shown in figure 2(c), indicates that $M_{bc} = gm(z_G - z_V) \sin \beta$, where the depths to the centres of volume and mass are z_V and z_G , respectively. The mean slope of the stratification is given as $\beta = 2z_T/L$. It is possible to derive W from L_N , albeit with a modified form – the thickness of the lower layer only vanishes from the parameterization for $h_2 \gg h_1$.

2.2. Transformation to normal-modes

The link between W and L_N and the first two normal modes suggested by Imberger & Patterson (1989) is arrived at by first assuming that (3) is calculated based upon the density interface immediately beneath the stress driven layer. The authors then describe a first mode response as being characterized by a small W and a small L_N and a second mode response as small W and large L_N . This may be quantified by considering how the transformation to normal modes is carried out for three layers.

Separation of variables allows a transformation from equations of motion for the individual layers to equations of motion for the modes (Csanady 1982; Monismith 1985, 1987). Thus, the layer equations of motion

$$\left. \begin{aligned} (u_j)_t &= -\frac{1}{\rho_0}(p_j)_x + f_{\tau j}, \\ (u_j)_x + \frac{(h_j)_t}{h_j} &= 0, \end{aligned} \right\} \quad (6)$$

become the modal equations of motion

$$\left. \begin{aligned} (U_i)_t &= -(P_i)_x + F_{\tau i}, \\ (U_i)_x + (P_i)_t &= 0. \end{aligned} \right\} \quad (7)$$

Here lower case refers to the layered variables and upper case to the modal equivalents, with x and t subscripts identifying differentiation. Thus, u_j , p_j and $f_{\tau j}$ represent the horizontal velocity, pressure and body-force in the j th layer whilst U_i , P_i and $F_{\tau i}$ are the velocity, pressure and body-force associated with the i th mode.

Equation (7) may be solved for the relevant boundary conditions which, in this case, are no flow through the boundaries and the surface stress acting as a body force in the upper layer. Finally, the layer velocities and interfacial displacements are found by inverting the original transform. Hence, the layer displacements have components due to each mode and, in particular, the displacement of the upper internal interface is

$$\zeta_1 = \zeta_1|_{bt} + \zeta_1|_{bc1} + \zeta_1|_{bc2}, \quad (8)$$

where the terms on the right-hand side represent the barotropic modal deflection $\zeta_1|_{bt}$ and the two baroclinic modal deflections, $\zeta_1|_{bc1}$ and $\zeta_1|_{bc2}$. In the same way as (3) compares the upwind interfacial deflection to the initial upper-layer thickness, (8) can be used to compare the deflection due to individual modes to the upper-layer thickness. The individual components of (8) are compared with h_1 at $x/L = 0$ and so that

$$\left. \begin{aligned} \frac{h_1}{\zeta_1|_{bt}} &= 2 \frac{\delta}{\gamma} \frac{H}{h_1 + h_2} \frac{gH h_1}{u_*^2 L}, \\ \frac{h_1}{\zeta_1|_{bc1}} &= 2(\beta_1 - \beta_2) \frac{gH h_1}{a_1 u_*^2 L}, \\ \frac{h_1}{\zeta_1|_{bc2}} &= 2(\beta_1 - \beta_2) \frac{gH h_1}{a_2 u_*^2 L}, \end{aligned} \right\} \quad (9)$$

where (see Csanady 1982)

$$\left. \begin{aligned} H &= h_1 + h_2 + h_3, \\ \gamma &= \frac{1}{H^2} (h_1 h_2 \epsilon_{12} + h_1 h_3 \epsilon_{13} + h_2 h_3 \epsilon_{23}), \\ \alpha &= \frac{h_1 h_2 h_3}{H^3} \epsilon_{12} \epsilon_{23}, \\ \delta &= (\gamma^2 - 4\alpha)^{1/2}, \\ \beta_{1,2} &= \frac{H}{2} (\gamma \pm \delta) + O(\epsilon_{13}^2 H), \\ a_i &= \frac{h_2 h_3}{\beta_i} \epsilon_{23} - (h_2 + h_3) + \beta_i \quad (i = 1, 2). \end{aligned} \right\} \quad (10)$$

It can be seen that the barotropic term $h_1/\zeta_1|_{bt}$ in (9) is approximately scaled by ϵ_{ij}^{-1} relative to the two baroclinic terms, and in the natural environment $\epsilon_{ij} = O(10^{-3})$, so that the barotropic displacement of the ζ_1 interface is approximately 10^3 times smaller than the baroclinic displacement. For the purpose of this expansion the barotropic component is ignored as it generates minimal interfacial deflection. The baroclinic terms $\zeta_1|_{bc1}$ and $\zeta_1|_{bc2}$ differ only by the a_i coefficients multiplying the shear stress term, u_*^2 . The a_i terms are the layer-to-mode transform variables for the forcing terms (Monismith 1985). It is proposed here that the distribution of energy between the first two baroclinic modes be estimated by comparing a_1 and a_2 . Thus, if the ratio a_2/a_1 is < 1 the first mode is expected to dominate whereas if $a_2/a_1 > 1$, then mode two should be large, assuming the stress exists for a sufficient duration. The ratio may be considered more closely if $h_1 \rightarrow 0$ then $a_1 \rightarrow 0$ and $a_2 \rightarrow \infty$ so that the second mode is favoured; conversely if $\epsilon_{23} \rightarrow 0$ then the ratio tends to 0. Thus, the ratio can be considered to follow W/L_N , although the actual relationship is more complex than

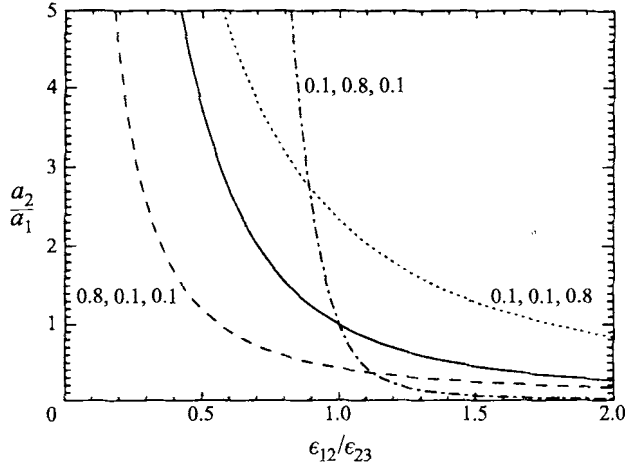


FIGURE 3. Curves showing variation of a_2/a_1 as a function of $\epsilon_{12}/\epsilon_{23}$ for different relative layer thicknesses.

this. Figure 3 illustrates these variations with curves of a_2/a_1 as a function of $\epsilon_{12}/\epsilon_{23}$ where ϵ_{13} is constant so that the changes are due to relative strengths of the upper and lower interfaces. Curves shown include those for three equal layers, and then two equal layers, with the third being much thicker. For equal layer thicknesses and equal density differences at the two interfaces the modal amplitudes are equal and as the density difference at the upper interface is emphasized the mode two response grows. The mode two response is also enhanced with thin upper layers, while a thick intermediate layer makes the ratio very sensitive to changes in the density distribution.

2.3. Unsteadiness

With more than one vertical wave mode the time-scales for maximum shear and tilt (i.e. $\frac{1}{4}T_1$ and $\frac{1}{2}T_1$, as identified by Spigel & Imberger 1980) are replaced by T_i where the index represents the i th vertical mode. The appropriate non-dimensional ratio delineating whether the wind duration is of sufficient duration to allow tilting due to the i th mode to fully develop is

$$\frac{4T_w}{T_i}, \quad (11)$$

where T_w is the wind duration. Table 1 compiles field observations of more notable events indicating that this ratio varies considerably in the natural environment. A practical consideration related to this growth timescale is that a u_* time-series should first be low-pass filtered with a filter time constant $\simeq \frac{1}{4}T_1$ before a time-series of W or L_N is calculated (Stevens *et al.* 1996).

As upwelling may be important to the development of the entrainment processes, it is useful to know how long after the start of a wind event the interfacial region is likely to reach the surface. An estimate of this is made by assuming that the vertical deflection of a given isopycnal at $x = 0$, $\zeta(z, t)$, once equilibrium has been reached, is given by

$$\zeta(z, \infty) \sim \frac{zT}{W}. \quad (12)$$

If the isopycnal deflection is assumed cosine-like in time and due to mode one only then

$$\zeta(z, t) = \zeta(z, \infty)[1 - \cos(2\pi t/T_1)]. \quad (13)$$

If the fluid upwells it follows that the time required for the isopycnal at depth z_T to reach the surface is

$$\frac{T_1}{2\pi} \arccos(1 - W). \quad (14)$$

Thus, the time-scale is a combination of the internal wave period and the surface layer stability. The W should be replaced with L_N if deep upwelling is being considered.

2.4. Non-hydrostatic and nonlinear effects

Any interfacial deflection that leads to upwelling will necessarily be comparable with the layer thicknesses and thus invalidate the assumption of small amplitudes. Consequently, the nonlinear and non-hydrostatic components of the momentum equation might simply become too large to ignore. The relative magnitude of the vertical acceleration may be estimated by comparing the vertical acceleration of the fluid, w_t , with the reduced gravitational acceleration ϵg . The comparison of these two terms may be developed as

$$\frac{w_t}{\epsilon g} \sim \frac{(h/L)u_t}{\epsilon g}.$$

Here the vertical velocity is replaced by $(h/L)u$ as the horizontal velocity is easier to measure. It is possible to show that $u \sim (h/L_N)(\epsilon g/h)^{-1/2}$ where h is an average layer thickness and $\partial/\partial t \sim 1/T_1$. After substitution one finds that $w_t/\epsilon g \sim (h/L)^2 L_N^{-1}$, implying a stronger dependence on the aspect ratio h/L than on L_N . Values of L_N considered in these experiments are between 0.2 and 3.2 and the surface-layer aspect ratio is approximately 0.05, suggesting that non-hydrostatic effects should be minimal and become even less important as the aspect ratio tends towards values probably found in the natural environment. It may be shown that the nonlinear terms scale in the same way, and so these too will be ignored.

3. Experimental details

The salt stratified experiments were carried out in a double glazed tank ($2.0 \times 0.4 \times 0.4 \text{ m}^3$), with a 20 mm thick Plexiglas floor as shown in figure 4(a). The double glazing reduced thermal convection through the sidewalls while the Plexiglas enabled conductivity and temperature probes to profile vertically from below. The surface stress was applied with a belt of mylar fabric coated with polystyrene balls (diameter $\approx 1.5 \text{ mm}$) freely suspended on one metre arms and was driven by a direct current motor (figure 4b). The actual stress imparted to the water surface was measured with a force transducer ($\pm 0.5 \text{ N}$, figure 4c) recording the reacting force imparted on the belt. The force output from the transducer was converted to the actual force acting on the water surface. The force transducer also served to reduce the steady-state horizontal belt deflection, consequently the average displacement of the belt frame was much less than 1 mm. A typical belt speed was $U_B = 160 \text{ mm s}^{-1}$, which in this case, gave a drag coefficient of $c_D = (u_*/U_b)^2 = 3.5 \times 10^{-3}$, and a ratio $U_b/u_* \approx 17$; this is comparable to the value of 20 used by Monismith (1986), given that the belt materials were different.

The stress was introduced linearly over a time comparable with half the first baroclinic period to reduce the effects of a very sudden stress application. During the initial portion of the belt acceleration, the boundary-layer beneath the belt was laminar, but once the belt reached a sufficient velocity, transition to turbulence occurred in the boundary-layer. Relative to the baroclinic timescales, the transition to turbulence occurred everywhere along the belt-water interface at the same time. The

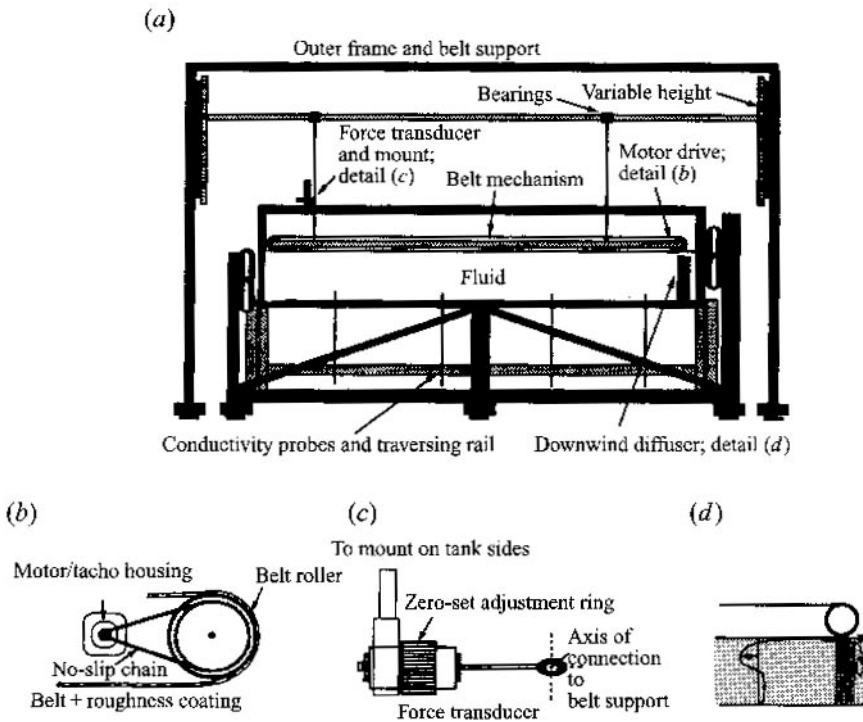


FIGURE 4. The experimental apparatus including, (a) the main tank, (b) the motor drive, (c) the force transducer moment and (d) the downwind diffuser.

polystyrene roughness elements were required so that the experiments could be run at convenient operating speeds. Removal of the roughness elements resulted in a boundary-layer transition to turbulence part-way along the belt, and consequently, an undesirably variable stress distribution.

Another phenomenon observed in initial trials (and Monismith 1986) was a current generated by the fast-flowing near-belt boundary layer; the fluid in this current would hit the down-wind endwall, turn downward as a jet-like flow, and erode the stratification at a rate at least comparable with the upwelling mechanism. This jet mechanism would be much less dominant in the field, as matching the field L_N parameter in the laboratory situation results in the Richardson's number associated with the laboratory surface flow being much smaller than in the corresponding flow in the natural environment. A downstream diffuser was installed (figure 4d) to dissipate the boundary-layer momentum in the laboratory experiments. It consisted of a 30 mm thick pad of synthetic horse-hair, with a small gap behind it. The arrangement caused the momentum to be lost in the thin vertical slot, at which point the fluid would move out into the main basin at its level of neutral buoyancy, and at much reduced velocities.

Data from each experiment typically consisted of periodic vertical profiles, at a frequency greater than four times the typical fundamental first-mode baroclinic frequency, of a rack of between four and six conductivity probes placed at various locations along the tank. The probes were four-electrode conductivity sensors (Head 1983) with a spatial resolution of 1 mm. The sensors were calibrated with an Anton-Paar density meter. Velocities were also measured, using a cross-correlation technique (Stevens & Coates 1994), where digitized video images of laser-illuminated aluminium flakes placed in the fluid were used to resolve both quantitative mean

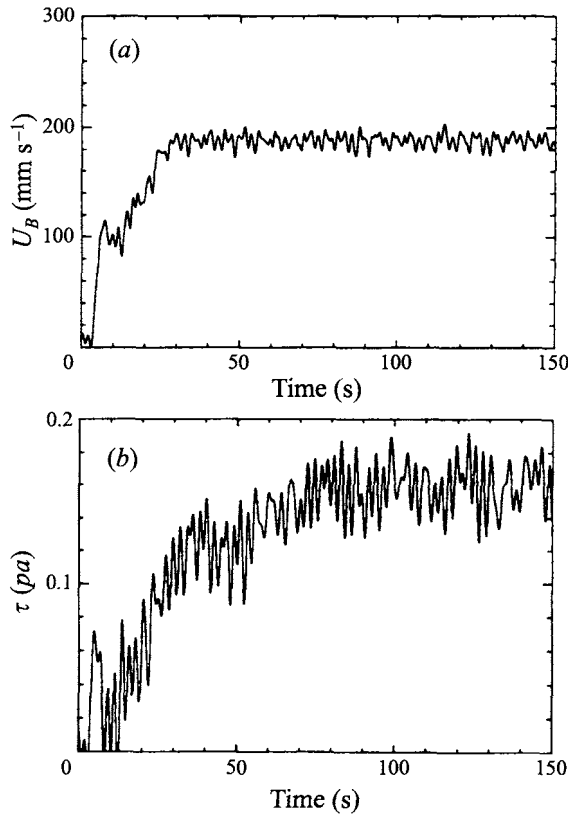


FIGURE 5. Example data showing how the measured belt stress and velocity compare with previous methods of calculation. The belt velocity U_b is plotted as a time-series in (a) and compares well with (b) the independently measured belt stress τ .

velocities and qualitative impressions of the turbulent fluctuations. The technique was limited by a maximum search radius so that, in this application, velocities greater than approximately 25 mm s^{-1} gave a spurious result. The fast horizontal flow near the belt (i.e. the top 10 mm) was often outside this limit. To compensate for this, the missing velocities in this region were replaced with estimates using a logarithmic boundary-layer model that matched the inner flow and the moving-belt boundary condition. The images from which the velocities were derived were 160 mm high and 80 mm wide and recorded at a position approximately $x/L = 0.33$ along the tank from the upwind endwall. As there was little variation of the velocity data across (in a longitudinal sense) the image, the data were horizontally averaged to improve the signal-to-noise ratio.

The belt velocity was computer controlled, with the output from a tachometer attached to the motor providing feedback for the control program. Typical tachometer output is shown in figure 5(a). The belt suspension system was undamped (except for the minimal damping provided by the force transducer), consequently the fluctuations in the applied stress were of the same amplitude as the mean signal. However, the natural oscillation period of the belt mechanism was much shorter than the seiche periods so that the stratified response is assumed to be a function of a filtered stress signal. A typical record is shown in figure 5(b); any decrease in the filter cut-off frequency removed the sharp response and note that even this filtered time-series has higher variability than the raw velocity data. All experiments used a constant total water depth of 160 mm, so that the barotropic period was around 3 s.

Calculation of W and L_N required knowledge of the applied stress and the density distribution so that measurement confidence may be derived from the reliability of the contributing data. The two largest sources of instrumentation error were that of the measured belt stress (proportional to u_*^2) and the density field. The stress measurement was in error because the force transducer allows a slight displacement from the equilibrium position. The resulting restoring force was estimated and included in the calculation for the force created by the belt. The reliability of the actual stress measurement was within 2%. The belt area was 96% of the water surface area of the tank and it is assumed that the deficit was of little importance as the edge regions were those most affected by boundary-layer regions. Again this was corrected for, resulting in a mean error of $\pm 5\%$ for the value of u_*^2 . The limitation in the density measurements was a combination of deviation from isothermal assumption, changes in the calibration of the probes and a lack of horizontal resolution. The departure from isothermal conditions was estimated to represent 2% of the measurement at worst. The conductivity probe measurements contain errors of around $\pm 5\%$. The probes deteriorated to this level over the course of the experiments and were more accurate in the earlier experiments. In addition, cross-calibration based on initial and final profiles improved the calibration. All lengthscales were assumed to have ± 1 mm error. Thus, the sum of the errors was about $\pm 7\%$.

Implicit in the work is that all the belt stress is balanced by the baroclinic moment, ignoring sidewall effects. Monismith (1986) estimated the error in W due to this assumption was around 5%. Here, rather than considering a circulation velocity ($\sim u_*$) as the velocity responsible for sidewall (and bottom) stress, an estimate is made based on the average baroclinic velocity. A first-order estimate shows that the ratio of the sidewall shear force F_{sw} , based on layer velocities, to belt shear force F_{belt} , was

$$\frac{F_{sw}}{F_{belt}} \approx c_D W^{-1} \frac{L h_1 h_2 (b + 2H)}{b H^3}, \quad (15)$$

where b is the tank width. Substituting typical values and, for comparison, the same friction coefficient that Monismith (1986) used ($c_D = 0.02$) then a numerical value for (15) is ≈ 0.1 – comparable to measurement errors.

The most significant source of uncertainty in the velocity analysis lies in the resolution inherent in the technique. The turbulence in the upper layer and advection due to circulation quickly removed particles from the field of view so that it was necessary to use a small timestep between images, resulting in poor velocity resolution in the slower-moving fluid layers. However, compromises were found which yielded the changing response. Velocities were only recorded at $x/L = 0.33$, requiring assumptions in how the flow varied along the horizontal extent of the tank. The assumptions are discussed later.

4. Experimental observations

The following section describes experiments with progressively decreasing L_N . The experimental data are listed in table 2.

4.1. The wave response; $L_N > 1$

Experiment E6 illustrates the fluid response when the stress is insufficient to bring the upper interface to the belt driven surface. The initial density profile and the normalized horizontal velocity associated with the first two baroclinic modes are shown in figures 6(a) and (b). With $L_N = 2.9$, $W = 0.9$ and a stress duration greater than $\frac{1}{4}T_2$, upwelling

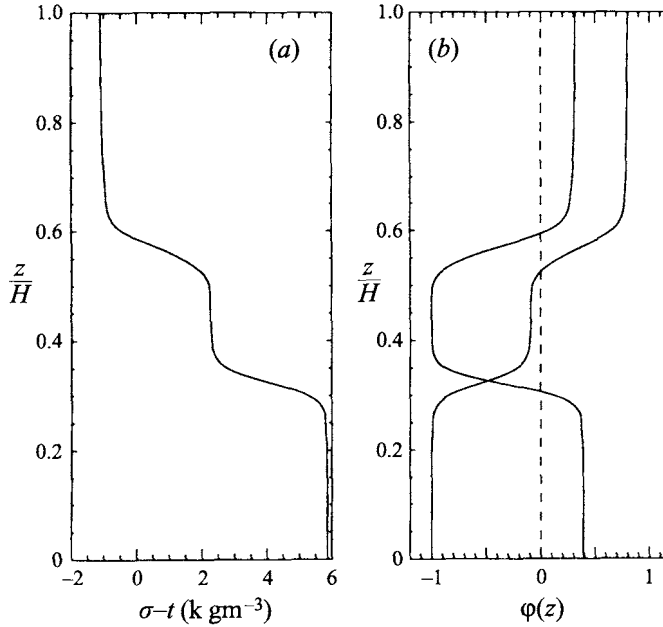


FIGURE 6. (a) Initial density profile for experiment E6 ($\sigma_i = \rho - 1000$) and (b) the calculated normalized horizontal velocity associated with the first two vertical modes.

Experimental data

Experiment	h_1 (m) ($\times 10^3$)	h_2 (m) ($\times 10^3$)	h_3 (m) ($\times 10^3$)	ϵ_{12} ($\times 10^3$)	ϵ_{23} ($\times 10^3$)	T_w (s)	T_1 (s)	T_2 (s)	u_*^2 (m s^{-1}) ² ($\times 10^4$)	W	L_N	a_2/a_1
E13				$N^2 = 0.7 \text{ (rad s}^{-1}\text{)}^2$			200	82	166	1.0	—	3.2 1.0
E6	67	42	51	3.14	3.6	210	86	167	0.84	0.9	2.9	1.0
E8	53	33	74	5.0	2.0	210	81	197	0.9	1.6	2.0	0.3
E10	60	20	80	3.1	3.2	200	84	235	0.88	1.3	2.0	1.1
E7	72	36	52	3.0	3.5	275	86	179	1.9	0.84	1.3	1.1
E14				$N^2 = 0.3 \text{ (rad s}^{-1}\text{)}^2$			200	141	280	1.0	—	1.3 1.0
E1	55	31	74	4.85	1.64	175	83	199	1.6	0.5	1.1	0.25
E4	30	60	70	3.0	2.8	170	103	171	1.0	0.28	0.89	2.6
E12				$N^2 = 0.15 \text{ (rad s}^{-1}\text{)}^2$			175	192	389	1.0	—	0.70 1.0
E9	59	29	72	4.7	1.9	165	81	214	3.0	0.57	0.63	0.3
E11	72	41	47	5.0	0.97	165	90	250	3.9	0.15	0.56	0.1
E5	52	34	74	3.22	1.37	230	100	241	2.3	0.2	0.50	0.3
E2	54	31	75	1.85	3.61	170	90	224	4.0	0.07	0.35	3.0
E3	52	37	71	0.73	1.9	160	128	325	4.0	0.05	0.17	5.5

TABLE 2. Tabulated experimental variables and parameters. The total depth of fluid, H , for all experiments was 160 mm, the individual layer depths are h_1 , h_2 and h_3 , from top to bottom. The normalized interfacial density anomaly is defined as $\epsilon_{ij} = (\rho_j - \rho_i)/\rho_0$ where ρ_i and ρ_j are upper- and lower-layer densities. T_w , T_1 and T_2 are the stress durations and the first and second mode uni-nodal seiche periods, respectively. The friction velocity, u_* , is the mean value taken during the steady period of the experiments and the parameters W , L_N and a_2/a_1 are described in the text. Several of the experiments use an initial linear density profile and they have their initial buoyancy frequency listed instead of the layer descriptors

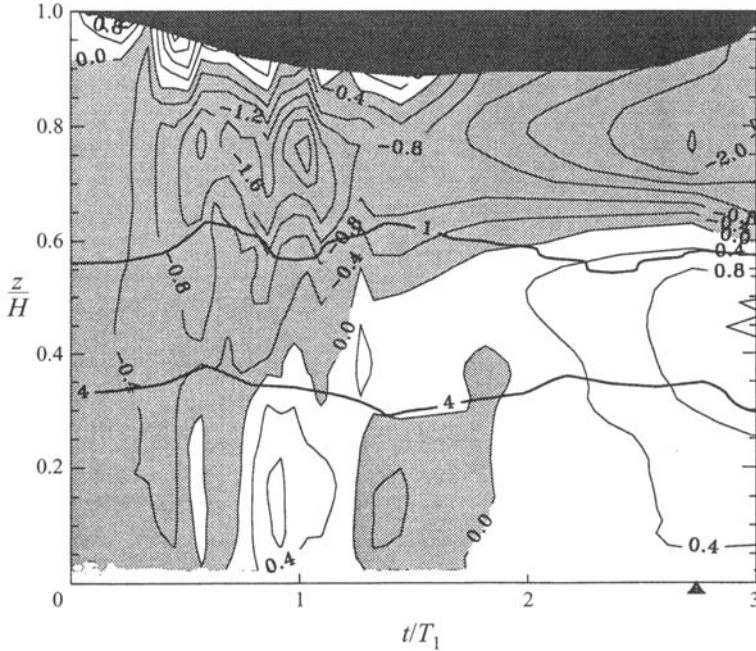


FIGURE 7. Contour plot combining normalized horizontal velocity at $x/L = 0.33$ and the $\sigma_t = 1$ and 4 kg m^{-3} isopycnals recorded at $x/L = 0.4$ for E6. The dark grey region represents data not recorded by the velocity detection scheme, the light grey region represents negative (upwind) velocities, whilst the white regions contain positive velocities.

is not expected and the second mode response should be apparent. Also, $a_2/a_1 \approx 1$ implies that after $\frac{1}{4}T_2$ a mode two amplitude that is comparable to mode one is expected.

The vertical profiles of the horizontal velocity, at $x/L = 0.33$, are shown as contours in figure 7, where positive velocities are oriented in the direction of the belt motion (i.e. 'downwind'). Initially a laminar boundary layer formed beneath the belt and both the thickness and mean velocity of the layer increased until around $t/T_1 = 0.23$, at which time the boundary-layer became turbulent. The penetration of the turbulent region into the upper homogeneous layer is discussed later. The return flow occurred between the base of the turbulent region and the bottom of the tank, and reached a peak normalized horizontal velocity of $u/u_* = -0.55$ (using the averaged u_* listed in table 2) at $t/T_1 = 0.3$. Three aspects of figure 7 should be considered. First, as mentioned in the previous section, velocity information could not be collected near the belt and is left blank in the contours. Secondly, the circulation within the upper layer caused a negative velocity flow to form between the upper interface and the belt driven positive flow. Thirdly, the two interface positions at $x/L = 0.4$, as represented by the $\sigma_t = 1 \text{ kg m}^{-3}$ and $\sigma_t = 4 \text{ kg m}^{-3}$ contours, undergo relatively minor deflections at this location. The density contours shown in figure 8(a-e) display the full spatial development at time intervals and the deflection is as described in Monismith (1986). The middle layer tilted, this was followed by the growth of upwind advection of the middle layer fluid and a subsequent flattening of the lower interface position. To assist in interpretation, the contours were constructed from sorted density profiles, eliminating overturns in the density structure. A caveat in contour interpretation is that, while contours through the turbulent surface layer have dynamic significance, they do not necessarily represent any contiguous baroclinic structure. The effect of this becomes more apparent at lower L_N .

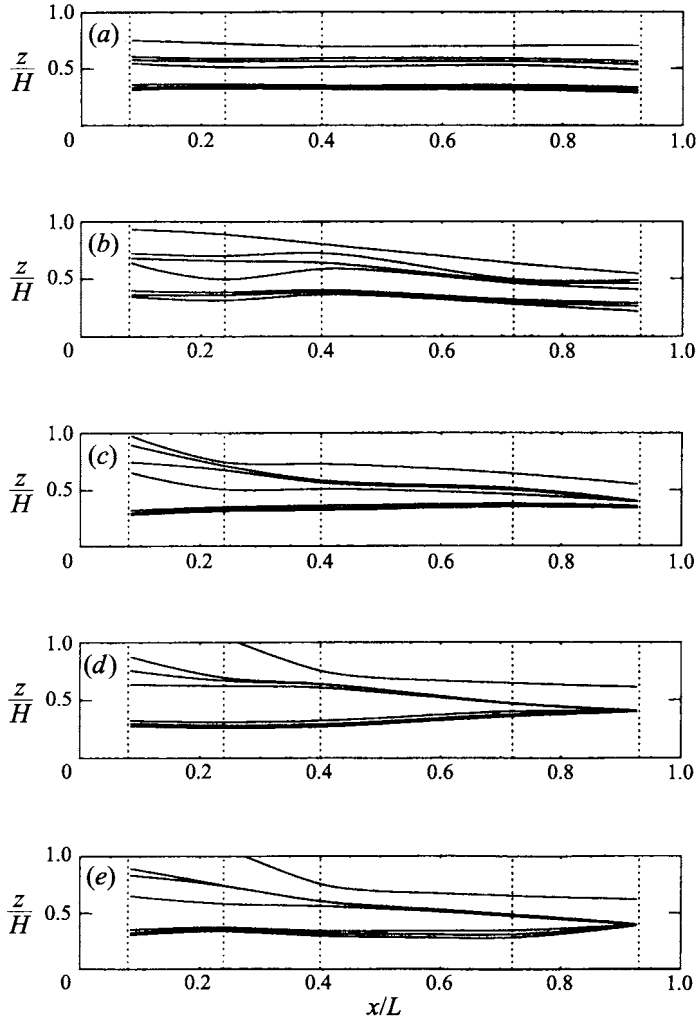


FIGURE 8. Contour plots at various times of the spatial distribution of the isopycnals from experiment E6 at times $t/T_1 =$ (a) 0.19, (b) 0.58, (c) 0.97, (d) 1.35, (e) 1.74. The contour intervals are set at 1 kg m^{-3} , with the deepest contour representing $\sigma_t = 5 \text{ kg m}^{-3}$.

While the observation that the response is a combination of internal modes is not surprising, a close examination of their relative development is warranted. To facilitate the comparison of the two baroclinic modes, the velocity profiles were integrated over the depth of the upper layer to remove the effect of the upper-layer circulation. Conceptually the amplitudes of the internal waves were estimated by minimizing

$$\int_0^H \left(\sum_{i=1,2} a_i \frac{\partial \phi_i}{\partial z} - \frac{\partial u}{\partial z} \right) dz, \quad (16)$$

where a_i are the free variables in the minimization that represent the modal amplitudes. The minimization can be applied to either discrete or continuous density profiles and modal functions ϕ_i . In practice the minimization was applied to the discretized profiles to reduce computation time. The non-dimensionalized layer-averaged horizontal velocities and the corresponding modal amplitudes, found using (16), are shown in

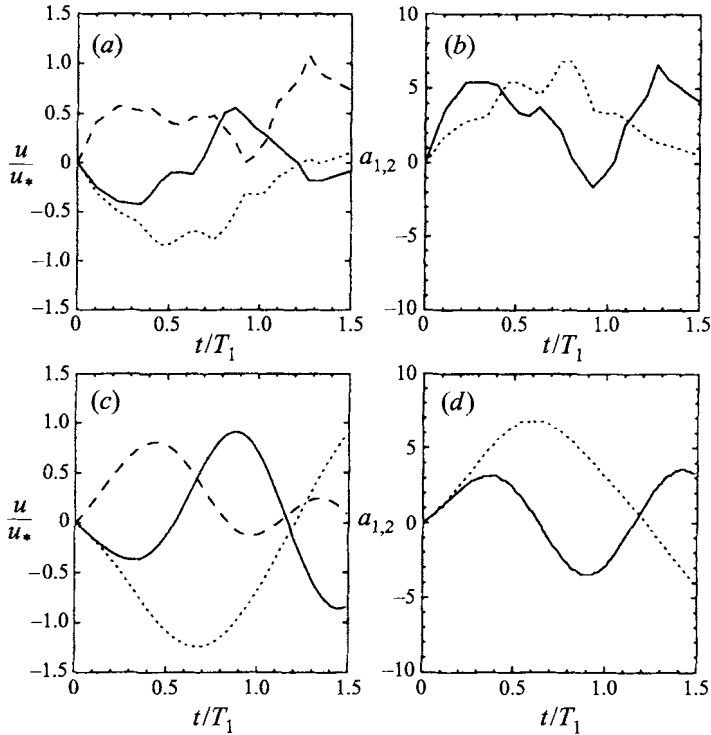


FIGURE 9. Results from E6 showing (a) layered averaged horizontal velocities at $x/L = 0.33$, where the upper, middle and lower layers are represented by dashed, dotted and solid lines respectively, (b) shows the modal amplitudes calculated with (16) where the solid line represents mode one and the dashed line, mode two. The three-layer model using parameters from E6 results in records of (c) layer horizontal velocities at $x/L = 0.33$ and (d) the modal amplitudes calculated with (16).

figures 9(a) and 9(b). The modal amplitudes show the anticipated growth in the first and second modes (cf. Monismith 1987) but not the first mode relaxation expected in the second half of T_1 .

The discretized stratification and the filtered stress distribution from E6 were used as input for the modal model described in §2. Figure 9(c) shows the model layer velocities, and comparison with figure 9(a) suggests the model works well in broad terms. As expected, the amplitudes were reduced in the laboratory observations owing to boundary effects and other losses not included in the simple model. The modal amplitude of the first mode was reduced in the second half-period in the laboratory observations; this seems to be associated with a surge in the upper layer at around $t/T_1 = 0.55$ (see figure 7). Seeking a reason for this surge, comparison with the circulation velocity and the distance from the downwind endwall suggests that it is the first turbulent fluid to return upwind that has come directly from the downwind endwall. Surge-like features are often associated with field observations of wind-driven internal waves (Thorpe 1977; Carmack *et al.* 1986).

Analysis of the energy budget for experiment E6 identifies where the work done by the stress was stored, if at all. The energy budget at a given time may be summarized as

$$E_r(t) = P_{bc}(t) + K_{bc}(t) + K_c(t) + K_{tke}(t) + E_L, \quad (17)$$

where E_r is the cumulative energy introduced into the system by the belt up until time t . The terms on the right-hand side represent the increase in potential energy P_{bc} of the

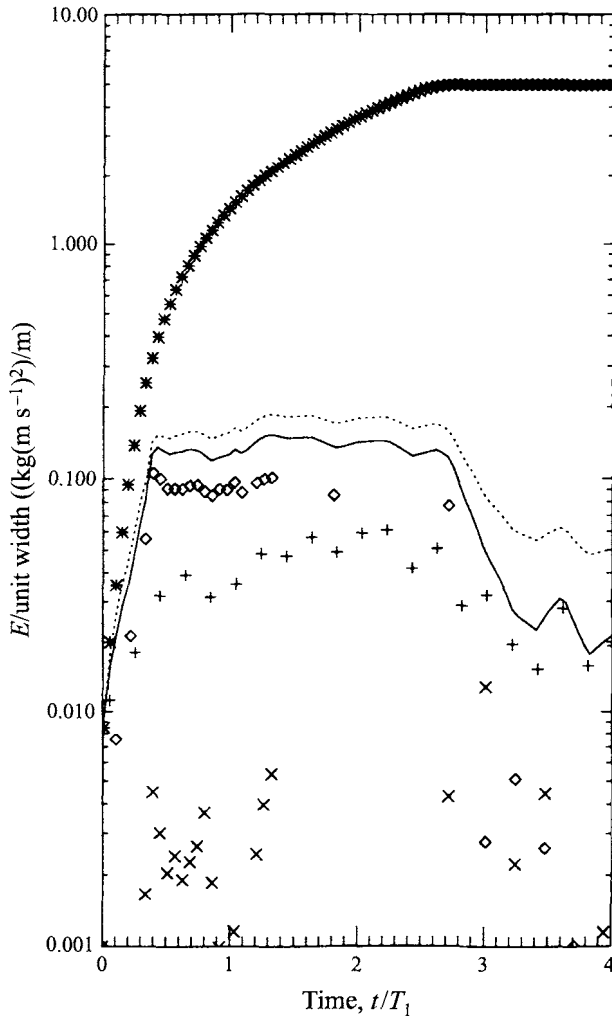


FIGURE 10. The energy budget for E6 showing \diamond , K_c ; \times , K_{bc} ; $+$, P_{bc} ; $*$, E_L as functions of non-dimensional time. The solid and dotted lines represent $K_c + K_{bc} + P_{bc}$ and $K_c + K_{bc} + P_{bc} + E_{tke}$, respectively.

water column, the kinetic energy K_{bc} held in the baroclinic oscillations, the kinetic energy K_c held in the surface-layer circulation, the total turbulent kinetic energy K_{tke} and, lastly, losses E_L from the system. Energy dissipation within the downwind endwall absorber is included here in the E_L term. The data allowed estimation of the first three terms on the right-hand side of (17) as shown in figure 10. The P_{bc} term was calculated by finding the potential energy per unit area at each profile and using these values to estimate the longitudinal average. Figure 11 shows the ratio of the energy including the absolute sum of spatial perturbations from the mean level of P_{bc} to P_{bc} itself, thus indicating energy stored in the seiche. From these data it is apparent that around 20% of the overall potential energy was held in the steady set-up of the internal structure. The peak to peak magnitude indicates that internal seiche held as much as 15% of the baroclinic potential energy. The kinetic energy in the circulation, K_c , was estimated by assuming that the horizontal velocity in the surface layer at the $x/L = 0.33$ position was representative of the flow throughout the tank. The baroclinic term, K_{bc} was

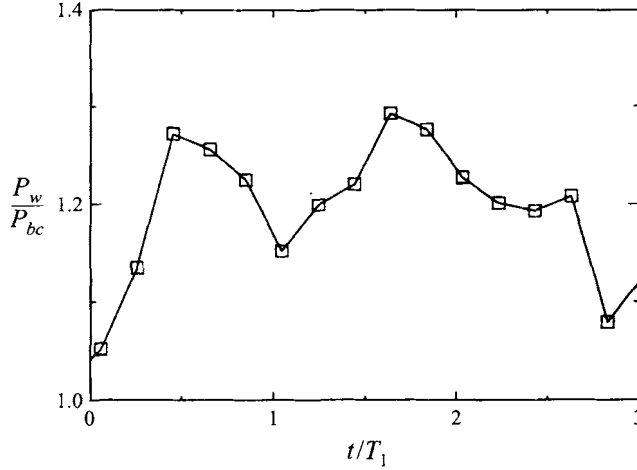


FIGURE 11. The ratio of potential energy including the internal wave structure to P_{bc} for experiment E6.

calculated by assuming that the velocity measured at $x/L = 0.33$ was a sample from a velocity field that varies as a half-wavelength of a sine function in space. The remaining quantities, K_{tke} and E_L , are unknown at this point.

The energy budget shows how little of the energy in the water column actually appeared as changes in the potential or kinetic energy associated with the baroclinic structure. In this experiment observed values of P_{bc} or K_{bc} were about one hundredth of E_r at any particular time. The majority of the energy that could be estimated directly was in K_c . If (17) is considered a reasonable approximation of the energy budget, the last two terms, E_{tke} and E_L can be estimated by assuming models for both. First, it is assumed that

$$E_{tke} = \int_0^L \int_0^h \frac{1}{2} \rho_0 u'^2 dz dx,$$

where u' is a characteristic turbulent velocity scale, and that the losses were all accounted for by turbulent dissipation (u'^3/l' , where l' is a characteristic turbulent lengthscale taken to be the depth of the surface layer) to heat. Then the losses can be modelled as

$$E_L = \rho_0 \int_0^L \int_0^h \frac{u'^3}{l'} dz dx.$$

By solving (17) for u' at each time step, then the majority of the energy must have been lost to viscous dissipation. Values of u' were around $2u_*$. This formulation of the E_L implies that energy lost from the system went first to E_{tke} , and was then dissipated (see Spigel, Imberger & Rayner 1986).

4.2. The combined wave-entrainment response; $L_N \approx 1$

Similar observations from the less stable experiment E1, where $L_N = 1.1$, $W = 0.5$ and $a_2/a_1 = 0.25$, illustrate upwelling where mode one dominates. However, linear modelling cannot reasonably be applied and mixing cannot be ignored. Figure 12 shows the velocity variations developed much as for E6, but at around $t/T_1 = 0.6$ the middle layer flow suddenly reversed and the flow became three-dimensional. In experiments where three-dimensional circulation was apparent (E1 was the most

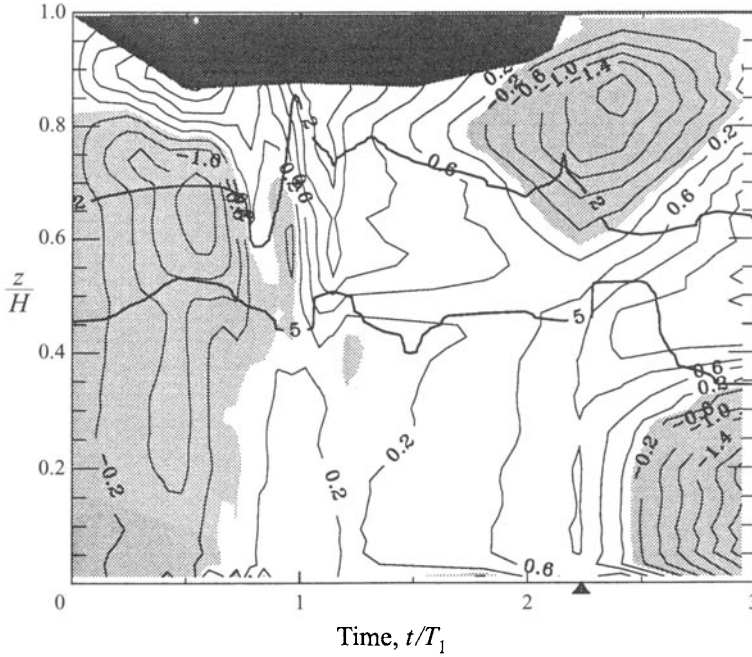


FIGURE 12. Contour plot combining normalized horizontal velocity at $x/L = 0.33$ and the $\sigma_t = 2$ and 5 isopycnals recorded at $x/L = 0.4$ for E1.

pronounced in this behaviour), two horizontal longitudinal gyres formed, with the mid tank velocity moving downwind. The density contours of figure 13 shows how sharp the upper interface remained until it reaches the surface at a time before $t/T_1 = 0.7$. The model velocities and modal amplitudes compared reasonably well with the observed data up until $t/T_1 = 0.6$, at which time mode one reached its maximum amplitude but mode two was only partially developed. As $a_1/a_2 = 0.25$, mode one should dominate, as the wind duration is sufficient for fully developed flow. The vigorous mixing after the interface reached the surface made a three-layer analysis, similar to that illustrated in figure 9, difficult and of little real value as the mixing rapidly shuts down further development of the modal dynamics.

Whilst the mean value of u_* for E1 was not greatly different from E6 there were some major differences in the energy budget (figure 14). First, K_{bc} was much larger, but still the smallest component of the assumed budget model. Also, in this experiment P_{bc} exceeded K_c for most of the experiment as the onset of upwelling increased the efficiency of the entrainment processes. The drop in the value of P_{bc} at the cessation of the belt stress ($t/T_1 \approx 2.2$) indicates that P_{bc} was boosted by the turbulent region which was not completely homogeneous over such short times and thus acted to suspend parcels of fluid above their levels of neutral buoyancy. The increase in P_{bc} , relative to the E6 energy budget, left less energy to be divided between K_{tke} and E_L .

The experiment E14, which had an initial linear stratification, but was in the same regime, developed in a similar fashion to E1, with a mixing layer extending along the full length of the tank. The fan-like structure observed by Monismith (1986) was again present as were short wavelength internal waves seen in E13 (Stevens & Imberger 1994).

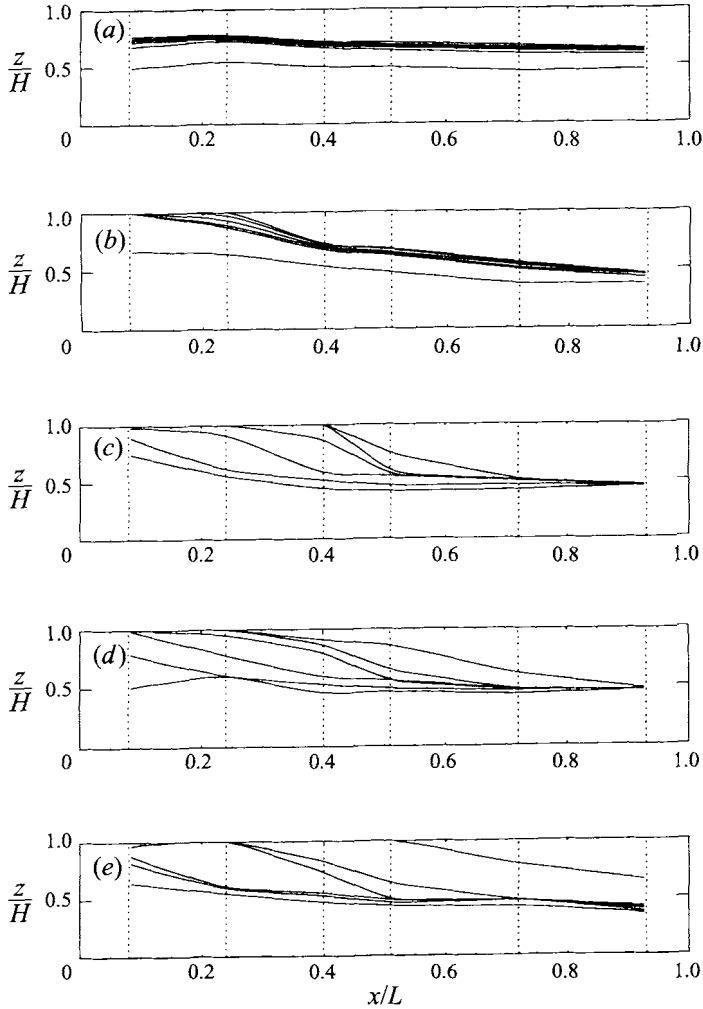


FIGURE 13. Contour plots at various times of the spatial distribution of the isopycnals from experiment E1 at times $t/T_1 =$ (a) 0.32, (b) 0.64, (c) 0.95, (d) 1.27, (e) 1.59. The contour intervals are set at 1 kg m^{-3} , with the deepest contour representing $\sigma_t = 5 \text{ kg m}^{-3}$.

4.3. The entrainment-damped response; $L_N < 1$

Little information is available in the literature in regard to very low stability experiments (see, however, Koseff & Street 1985). Typical of this regime was experiment E2, which had a $L_N = 0.35$, $W = 0.07$ and $a_2/a_1 = 3.0$. Parameterization indicates that entrainment and circulation dominate the behaviour as the density structure is very weak. As discussed by Spigel & Imberger (1980) the entrainment is partially driven by the extreme baroclinic tilting. Figure 15 shows that the surface-layer circulation entrained what was initially the middle layer (i.e. at time $t/T_1 = 0.3$ and $z/H = 0.65$) and continued to erode the deeper layer (figure 15), until around $t/T_1 = 1.0$, at which time the density contours of figure 16 show that most of the lower fluid had moved into the upwelling region; the turbulent surface layer extended over the full depth of the fluid at the down-wind end. The density structure did not change a great deal from that shown in figure 16(e), except that the surface layer was progressively homogenized. None of the experiments completely mixed the water column in the

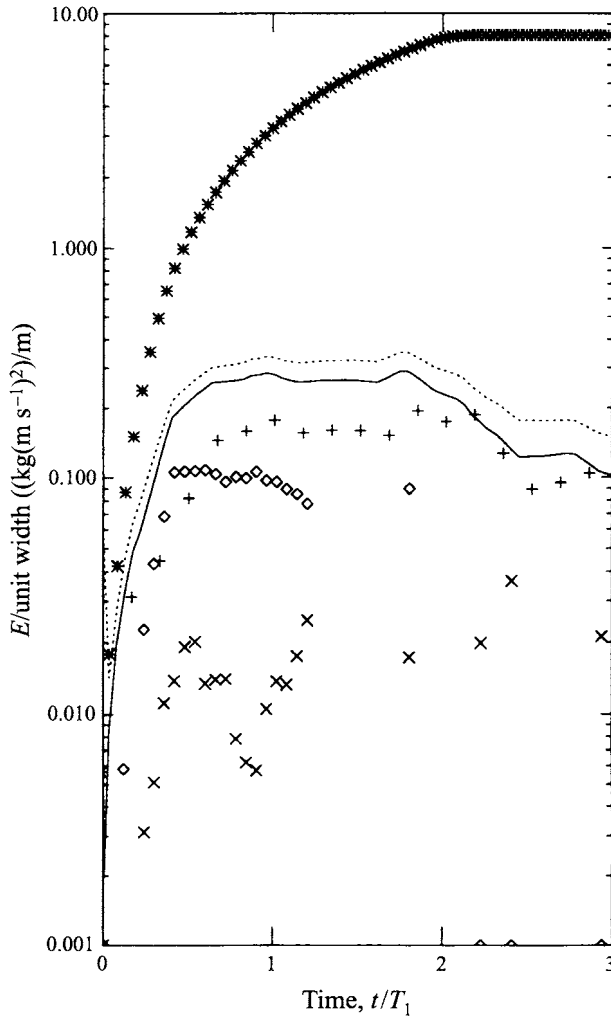


FIGURE 14. The energy budget for E1 with the same symbols as figure 10.

given T_w . The a_2/a_1 ratio implies a very strong mode two response. This experiment demonstrated that active mixing causes a general cessation of the long period mode two response. The energy budget (figure 17) showed that even the dominating first mode tilt is not enough to make K_{bc} a substantial part of the energy budget. As in E6, P_{bc} was smaller than K_c , despite the upwelling. The energy lost to dissipation dominated the energy budget and accounted for all but a few per cent by the end of the experiment. The calculated u' was again around $2u_*$.

The effectiveness of upwelling in this part of the parameter space ($L_N < 1$) is illustrated with figure 18(a), which shows the flow at the upwind endwall, again in an experiment similar to E2. The interpretative sketch (figure 18b) shows the commencement of upwelling where the flow was vertical near the wall and was subsequently dragged downstream by the belt-driven boundary layer.

The linearly stratified equivalent, E11, behaved in a similar fashion. The turbulent surface layer penetrated to the base of the fluid at the downwind end of the tank, similar to the contours shown in figure 16 and the tilting was so strong that fluid

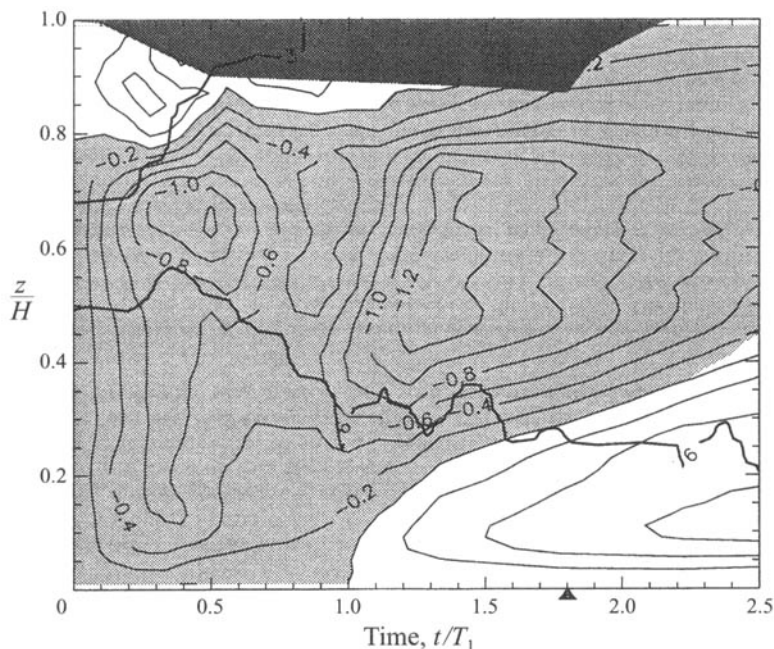


FIGURE 15. Contour plot combining normalized horizontal velocity at $x/L = 0.33$ and the $\sigma - t = 3$ and 6 isopycnals recorded at $x/L = 0.4$ for E2.

outside of the turbulent layer extended over a significant proportion of the surface of the tank in the same manner as illustrated in figure 18(a).

5. Discussion

5.1. Initiation of the surface stress

In all experiments, in the period just after the belt started to move, the barotropic wave created a surface pressure gradient and the turbulent generated by the belt quickly extended to the base of the surface layer. The vertical propagation velocity of the turbulent region into the initially homogeneous upper layer is shown in figure 19 for the section $0.33 < x/L < 0.4$. A linear least-squares fit yielded a slope of 0.16; this is less than that found by Sherman, Imberger & Corcos (1978) in a review of experiments, but it is in general agreement with expectations.

The largest return velocities in the surface layer were no greater than $2u_*$, accordingly the recirculation timescale (u_*/L) was greater than T_1 for most of the experiments in this study. Thus, the return flow at the base of the surface layer was initially associated with the baroclinic pressure wave, owing to the stress initialization, travelling along the interface in the upwind direction. This type of response was apparent, though not always, in field data recorded in Loch Ness and described by Thorpe (1977). However, the speed of turbulent vertical penetration of the surface layer relative to the baroclinic wave celerity, was considerably slower in the field observations when compared to the laboratory situation.

The bore remarked on in §4.1 requires some comment with respect to observation. As the approximate analysis showed, it was probably the front associated with the arrival of fluid from the downstream end of the tank. The front was even more apparent in the upwelling experiment E1, especially as it heralded the appearance of

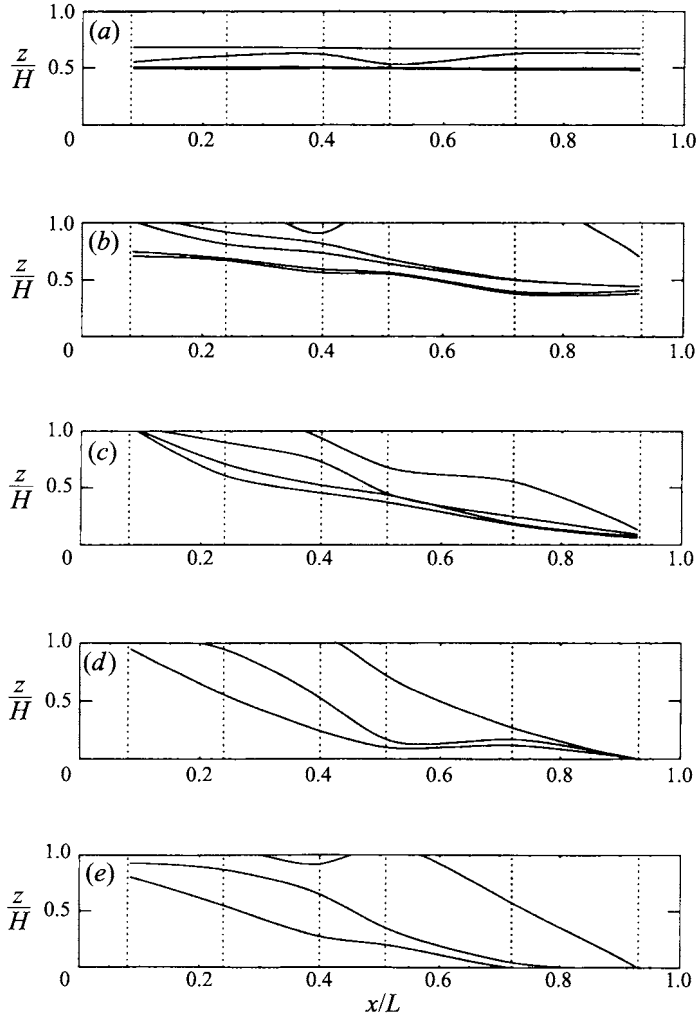


FIGURE 16. Contour plots at various times of the spatial distribution of the isopycnals from experiment E2 at times $t/T_1 = (a) 0.16, (b) 0.48, (c) 0.80, (d) 1.11, (e) 1.43$. The contour intervals are set at 1 kg m^{-3} , with the deepest contour representing $\sigma_t = 7 \text{ kg m}^{-3}$.

three-dimensional gyres. However, it was not obvious in the velocity contours of E2. It is possible that the brief slowing around $t/T_1 = 0.9$ is associated with the front, in keeping with the higher L_N experiments. However, more likely, is that the very fast circulation in the lower layer dominated any signal from the front. The implication is then that the circulation velocity will be much reduced in the field scale and that this parcel of fluid generated at the downwind end at the commencement of the wind might then be left to adjust baroclinically. This would be in keeping with internal bore observations mentioned previously. So mixing considerations might also need examination to explain limnological internal wave spectra.

5.2. Commencement of upwelling

The density contours allowed estimation of the time, T_u , at which the interfacial layer reached the free surface. Here the effect of ramping the belt speed was compensated for

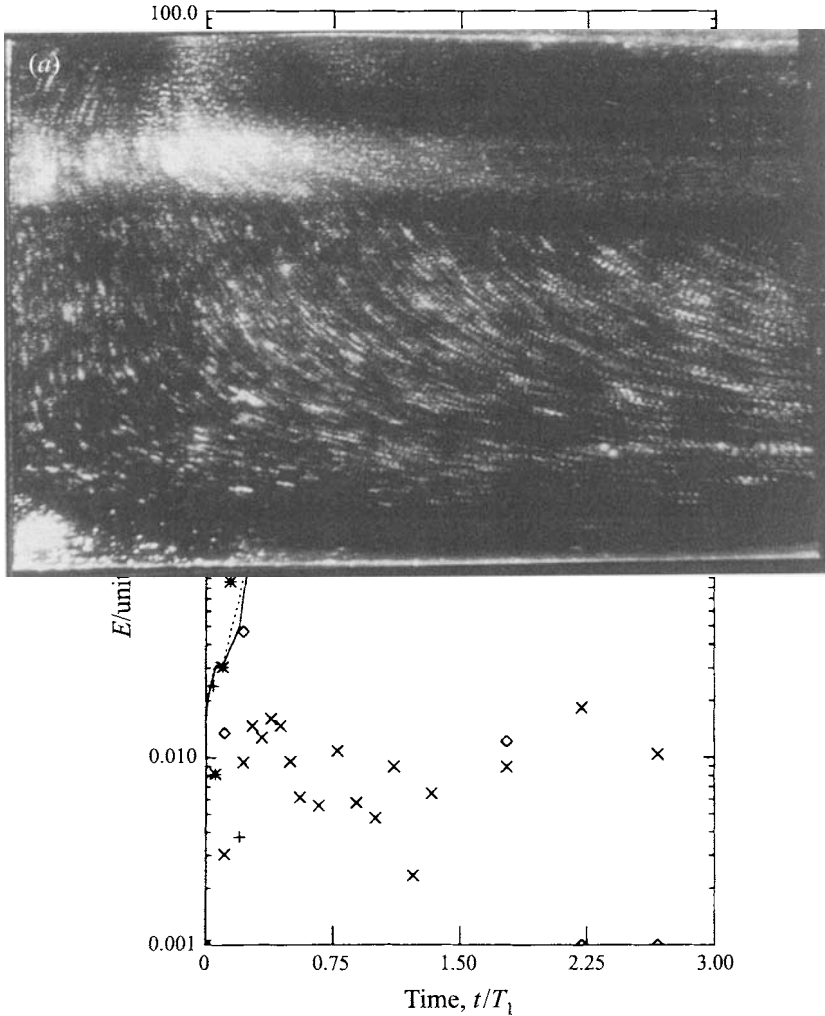


FIGURE 17. The energy budget for E2 with the same symbols as figure 10.

by assuming an average u_* rather than a peak; thus the modelled time of arrival is increased by a factor of four. Figure 20 compares the observations against the corrected estimate (14); the error bars represent half the time between profiles. The comparison was generally good, although four experiments fell outside the expected domain. These were, from left to right in figure 20, E4, E11, E1 and E8. Both E4 and E11 had small W so that their upper interfaces were weak and upwelling was more difficult to identify. E1 generated significant three-dimensional motion as described earlier and E8 behaved in a similar fashion to E6 in that upwelling *per se*, was not clearly observed, but some deeper fluid was apparent in density profiles.

The effectiveness of upwelling is illustrated by figure 21 which shows how a bulk entrainment efficiency, η , varies with L_N . The efficiency is described by

$$\eta = \frac{P_{bc}}{E_r}$$

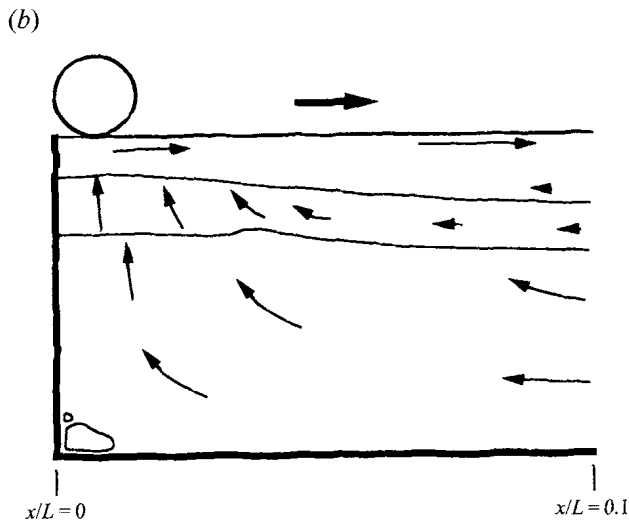
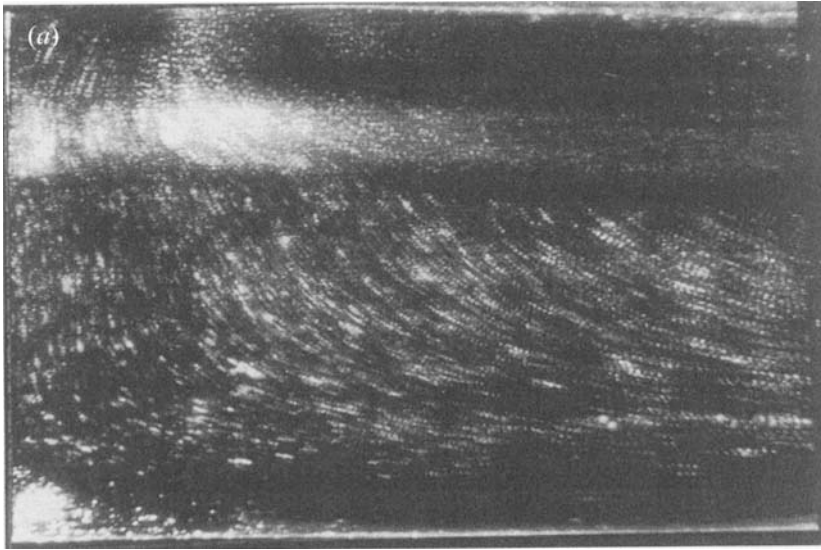


FIGURE 18. (a) Particle paths near the upwind endwall in an experiment similar to E2, taken at approximately $0.3t/T_1$ and (b) an interpretation sketch.

The increase in the potential energy was calculated, as before, with

$$P_{bc} = \int_0^L \int_0^H (\rho - \rho_0) g z \, dz \, dx.$$

The work imparted by the belt is

$$E_\tau = \rho_0 A \int_0^T U_b u_*^2 \, dt,$$

where $\int U_b u_*^2 \, dt$ is the temporal integral of the work done by the belt (belt speed scaled by friction velocity squared). The relative efficiency, η , gave values between less than

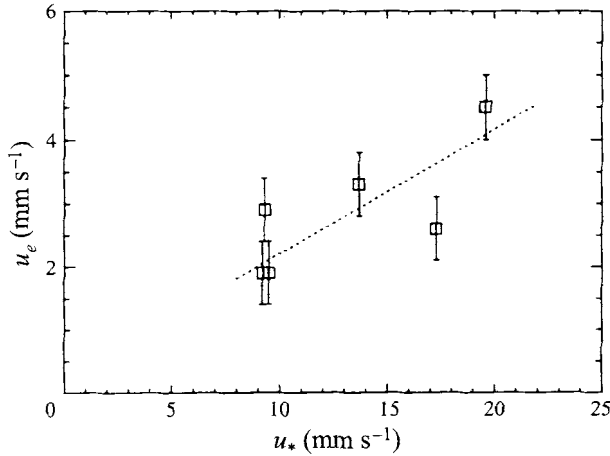


FIGURE 19. Penetration of the turbulent region at the start of the experiments, from E6 \rightarrow E11. Video of early experiments was not recorded in a manner enabling this analysis. Slope of least squares linear fit = 0.20.

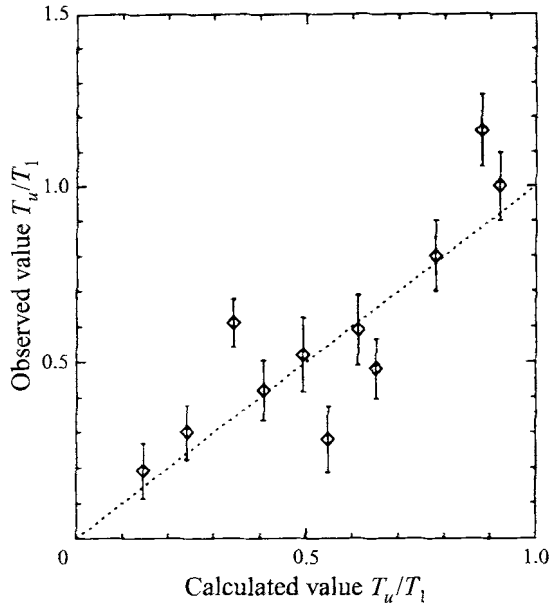
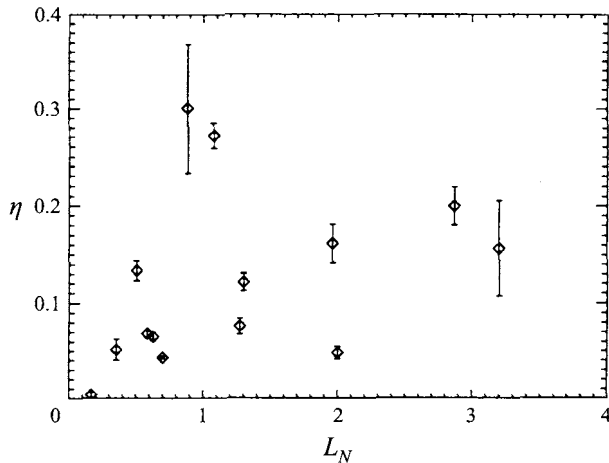


FIGURE 20. Comparison of the apparent time of upwelling and that suggested by (14).

1% and just over 30% when considering only the first $\frac{1}{2}T_1$. The results of this calculation are plotted in figure 21. Despite the scatter, the trend is apparent, with peak efficiency at $L_N \approx 1$; the efficiency drops markedly for the smaller L_N experiments and maintains lesser efficiencies for $L_N > 1$. The error bars are associated with lack of certainty in the density data and were thus enhanced as the change in the P_{bc} increased relative to E_r .

5.3. Parameterization

The W , L_N , T_w/T_i parameterization domain used in this paper describes the flow development. This description is achieved by calculating T_i , L_N , W , and a_2/a_1 . The response can be split into four categories. (i) If both W and L_N are large (≥ 1) then

FIGURE 21. Bulk efficiency η as a function of L_N .

only small-amplitude seiching will occur regardless of the T_w . (ii) If $L_N \gg 1$ but now $W < 1$ then, if T_w is sufficiently long, a mode two response should be seen with only small-scale deeper seiching. An upwelling timescale can be calculated for this. (iii) If the reverse situation is true with $W \gg 1$ and $L_N < 1$ little mixing at the upper interface is expected but deep seiching is possible with no upwelling. (iv) Finally, if both $W \ll 1$ and $L_N \ll 1$, then large-scale tilting is expected, especially if the wind persists for $\frac{1}{4}T_1$ and upwelling will halt the second mode growth as it changes the density structure of the fluid.

The sensitivity of the relative modal amplitudes to the layer thicknesses is important. Two studies that provide some of the clearest field observations of mode two internal waves are those of Wiegand & Chamberlain (1987) and Münnich, Wüest & Imboden (1992), and both studies observe a broad thermocline region (corresponding to a thick middle layer here). This leaves the relative modal response open to quite strong changes with small shifts in the density structure. One would expect the upper density step to change on a day-to-day basis with local weather patterns. This must result in a highly variable modal response.

Furthermore, in the natural environment, conditions often occur where the stratification contains a very shallow surface layer and thus W is small – suggesting strong mixing throughout the upper part of the water column. In reality, vertical entrainment must change the layer structure rapidly, quickly increasing the parameterized stability of the fluid. The behaviour is illustrated by comparing the timescale for the upper layer to double its depth solely through vertical entrainment, based on Kranenburg's (1985) model where non-dimensional vertical entrainment is proportional to $u_*^2/(egh_1)$, with the timescale for upwelling given by (14). From this entrainment law, the ratio of the time for upwelling to occur compared to the time for surface-layer doubling, owing to vertical entrainment, is

$$\frac{T_u}{T_*} \sim W^{-3/2} \left(\frac{h_1}{L(1-h_1/H)} \right)^{1/2} \arccos(1-W). \quad (18)$$

Thus, for a given wind event, if this ratio drops below one, upwelling occurs before vertical entrainment significantly changes the stratification. For typical stratification used in these experiments, a $W = 1$ results in T_u/T_* of around 0.5 so that upwelling can

occur. However, as W drops to around 0.5, vertical entrainment dominates. This functionality implies that decreasing the upper-layer thickness actually decreases the T_u/T_* so that upwelling still plays a part in mixing very shallow surface layers.

The effects of different endwall configurations and adjoining basins were identified as areas requiring further work as part of this general topic. In addition, relevant field observations rarely contain wind events that would be considered isolated, so that the effect of repeated, and even opposing, wind events, would extend understanding in this area.

6. Conclusions

From the experimental point of view, the present set of data provides new stress and velocity information. In addition, a good deal of the information comes from a region in the parameterization that has received little attention previously. With respect to the flow development, the major conclusions may be summarized as follows. (i) Mode two growth has been identified through analysis of velocity data. (ii) The relative modal response was most sensitive to density variations if the middle layer was relatively thick. (iii) An important component of the transient response was the advection of the turbulent fluid recirculating from the down-wind endwall at start-up. If the L_N was sufficiently large, the front of this flow was observed to travel the full length of the fluid. (iv) The internal wave response to the stress ceased once significant upwelling occurred. (v) Even though the wave response was effectively retarded by upwelling, the time at which upwelling occurred could still be estimated from the wave response as this was initiated prior to upwelling. (vi) Energy budgets indicated that upwelling was linked to overall effectiveness of mixing. A practical consideration drawn from the work is that the filtering of wind stress data using low-pass filter constants based on frequency cut-off at $\frac{1}{4}T_1$ is important for useful results.

The authors would like to thank John Taylor, Gregory Ivey, Michael Coates, John Patterson, Stephen Monismith, Robb McDonald, Gregory Lawrence and Tracy Farr for valuable discussions relating to this manuscript. The anonymous reviewers provided insightful and constructive criticism. John Bagrie was responsible for construction of the apparatus. This work was supported by an Australian Postgraduate Research Award, the Centre for Water Research and the Australian Research Council, and forms Centre for Water Research contribution ED466.

REFERENCES

- CARMACK, E. C., WIEGAND, R. C., DALEY, R. J., GRAY, C. B., JASPER, S. & PHARO, C. H. 1986 Mechanisms influencing the circulation and distribution of water mass in a medium residence-time lake. *Limnol. Oceanogr.* **31** (2), 249–265.
- CSANADY, G. T. 1982 On the structure of transient upwelling fronts. *J. Phys. Oceanogr.* **12**, 84–96.
- HEAD, M. J. 1983 The use of miniature four-electrode conductivity probes for high resolution measurement of turbulent density or temperature variations in salt-stratified flows. PhD thesis, University of California, San Diego.
- HEAPS, N. S. & RAMSBOTTOM, A. E. 1966 Wind effects on water in a narrow two-layered lake. *Phil. Trans. R. Soc. Lond. A* **259**, 391–430.
- HELLSTRÖM, B. 1941 Wind effect on lakes and rivers. *Ing. Vetensk. Akad. Handlingar*, NR158, 191 pp.
- IMBERGER, J. 1985 The diurnal mixed layer. *Limnol. Oceanogr.* **30** (4), 737–770.
- IMBERGER, J. & PATTERSON, J. C. 1989 Physical Limnology. *Adv. Appl. Mech.* **27**, 303–473.
- ISHIKAWA, T. & TANAKA, M. 1993 Diurnal stratification and its effect on wind-induced currents and water qualities in Lake Kasumigaura. *J. Hydraul. Res.* **31** (3), 307–322.

- KOSEFF, J. R. & STREET, R. L. 1985 Circulation structure in a stratified cavity flow. *J. Hydraul. Engng ASCE* **111** (HY2), 334–354.
- KRANENBURG, C. 1985 Mixed-layer deepening in lakes after wind set-up. *J. Hydraul. Div. ASCE* **111** (HY9), 1279–1297.
- LA ZERTE, B. D. 1980 The dominating higher order vertical modes of the internal seiche in a small lake. *Limnol. Oceanogr.* **25** (5), 846–854.
- MONISMITH, S. G. 1985 Wind-forced motions in stratified lakes and their effect on mixed layer shear. *Limnol. Oceanogr.* **30** (4), 771–783.
- MONISMITH, S. G. 1986 An experimental study of the upwelling response of stratified reservoirs to surface shear stress. *J. Fluid Mech.* **171**, 407–439.
- MONISMITH, S. G. 1987 Modal response of reservoirs to wind stress. *J. Hydraul. Div. ASCE* **113** (HY10), 1290–1306.
- MORTIMER, C. H. 1953 The resonant response of stratified lakes to wind. *Schweiz. Z. Hydrol.* **15**, 94–151.
- MÜNNICH, M., WÜEST, A. & IMBODEN, D. M. 1992 Observations of the second vertical mode of the internal seiche in an alpine lake. *Limnol. Oceanogr.* **37** (8), 1705–1719.
- SHERMAN, F. S., IMBERGER, J. & CORCOS, G. M. 1978 Turbulence and mixing in stably stratified waters. *Ann. Rev. Fluid Mech.* **10**, 267–288.
- SPIGEL, R. H. & IMBERGER, J. 1980 The classification of mixed-layer dynamics in lakes of small to medium size. *J. Phys. Oceanogr.* **10**, 1104–1121.
- SPIGEL, R. H., IMBERGER, J. & RAYNER, K. N. 1986 Modeling the diurnal mixed layer. *Limnol. Oceanogr.* **31** (3), 533–556.
- STEVENS, C. L. & COATES, M. J. 1994 Applications of a maximised cross correlation technique for resolving velocity fields in laboratory experiments. *J. Hydraul. Res.* **32** (2), 195–212.
- STEVENS, C. & IMBERGER, J. 1994 Downward propagating internal waves beneath the surface layer of a stratified fluid. *Geophys. Res. Lett.* **21** (5), 361–364.
- STEVENS, C. L., LAWRENCE, G. A., HAMBLIN, P. F. & CARMACK, E. C. 1996 Wind forcing of internal waves in a long narrow stratified lake. *Dyn. Atmos. Oceans*, **24**, 41–50.
- STUMM, W. 1985 *Chemical Processes in Lakes*. Wiley-Interscience.
- THOMPSON, R. O. R. Y. & IMBERGER, J. 1980 Response of a numerical model of a stratified lake to a wind stress. *Proc. 2nd Intl Symp. Stratified Flows, Trondheim*, vol. 1, pp. 562–570.
- THORPE, S. A. 1977 Turbulence and mixing in a Scottish loch. *Phil. Trans. R. Soc. Lond. A* **286**, 125–181.
- VAN SENDEN, D. C. & IMBODEN, D. M. 1989 Internal seiche pumping between sill-separated basins. *Geophys. Astrophys. Fluid Dyn.* **48**, 135–150.
- WEDDERBURN, E. M. 1912 Temperature observations in Loch Earn, with a further contribution to the hydrodynamical theory of the temperature seiche. *Trans. R. Soc. Edin.* **48**, 629–695.
- WIEGAND, R. C. & CHAMBERLAIN, V. 1987 Internal waves of the second vertical mode in a stratified lake. *Limnol. Oceanogr.* **32** (1), 29–42.
- WU, J. 1973 Wind induced entrainment across a stable density interface. *J. Fluid Mech.* **61**, 257–287.